A Combined Satellite Infrared and Passive Microwave Technique for Estimation of Small-Scale Rainfall

MARTIN C. TODD

Department of Geography, University College London, London, United Kingdom

CHRIS KIDD

School of Geography, University of Birmingham, Birmingham, United Kingdom

DOMINIC KNIVETON

Department of Geography, University of Leicester, Leicester, United Kingdom

TIM J. BELLERBY

Department of Geography, University of Hull, Hull, United Kingdom

(Manuscript received 8 March 2000, in final form 20 July 2000)

ABSTRACT

There are numerous applications in climatology and hydrology where accurate information at scales smaller than the existing monthly/2.5° products would be invaluable. Here, a new microwave/infrared rainfall algorithm is introduced that combines satellite passive microwave (PMW) and infrared (IR) data to account for limitations in both data types. Rainfall estimates are produced at the high spatial resolution and temporal frequency of the IR data using rainfall information from the PMW data. An IR_{Tb}–rain rate relationship, variable in space and time, is derived from coincident observations of IR_{Tb} and PMW rain rate (accumulated over a calibration domain) using the probability matching method. The IR_{Tb}–rain rate relationship is then applied to IR imagery at full temporal resolution.

MIRA estimates of rainfall are evaluated over a range of spatial and temporal scales. Over the global Tropics and subtropics, optimum IR thresholds and IR_{Tb}–rain rate relationships are highly variable, reflecting the complexity of dominant cloud microphysical processes. As a result, MIRA shows sensitivity to these variations, resulting in potentially useful improvements in estimate accuracy at small scales in comparison to the Geostationary Operational Environmental Satellite Precipitation Index (GPI) and the PMW-calibrated Universally Adjusted GPI (UAGPI). Unlike some existing PMW/IR techniques, MIRA can successfully capture variability in rain rates at the smallest possible scales. At larger scales MIRA and UAGPI produce very similar improvements over the GPI. The results demonstrate the potential for a new high-resolution rainfall climatology from 1987 onward, using International Satellite Cloud Climatology Project DX and Special Sensor Microwave Imager data. For real-time regional or quasi-global applications, a temporally ''rolling'' calibration window is suggested.

1. Introduction and background

There are numerous applications in meteorology, climatology, and hydrology where accurate estimation of rainfall at relatively small spatial and temporal scales (daily or subdaily estimates at resolutions of 1° down to the pixel scale) would be invaluable. There is also increasing demand from the climate community for such products over extended periods. High-resolution rainfall information is available for limited areas using combinations of ground-based radar and dense networks of rain gauges. For large areas of the globe, however, the in situ infrastructure necessary for this form of precipitation monitoring network is not in place. In addition, radar data can suffer from inconsistencies related to, among others, geometric considerations (Kidd 1997). Although global precipitation products at monthly/2.5° resolution derived from satellite data [and more recently a combination of satellite, rain gauge, and numerical weather prediction (NWP) data] are now routinely available (Huffman et al. 1997; Xie and Arkin 1997), there is an absence of global rainfall information at smaller

Corresponding author address: Martin Todd, University Lecturer, Department of Geography, University College London, 26 Bedford Way, London WC1H 0AP, United Kingdom.
E-mail: m.todd@geog.ucl.ac.uk

scales and over extended periods. Only since 1996 have daily/1° satellite/infrared (IR) products using the Geostationary Operational Environmental Satellite (GOES) Precipitation Index (GPI) been archived under the auspices of the Global Energy and Water Cycle Experiment (GEWEX) program (GEWEX 1996).

Satellite-based precipitation monitoring techniques are well established. However, accurate estimation of rainfall at such small spatial and temporal scales presents problems for satellite-based methods [see Barrett and Beaumont (1994) and Kidd et al. (1998) for a general review]. Satellite passive microwave (PMW) algorithms and, more recently, satellite-borne rain radar are able to provide accurate estimation of instantaneous rain rates, but the poor temporal sampling of low earth-orbiting satellites makes these techniques most suitable for estimation of accumulated rainfall over longer periods of perhaps a month or more. Moreover, it is well known that estimates from polar-orbiting satellites are subject to bias in regions where the diurnal cycle of rainfall is pronounced (Morrissey and Janowiak 1996). Imagery from geostationary satellite systems, when compared to polar-orbiting satellite data, generally results in a reduction of the sampling errors at all temporal scales. Accordingly, at the present time, estimates of global tropical and subtropical rainfall at short timescales (from a few hours to perhaps a few weeks) are most accurately obtained from geostationary satellites. Although passive microwave sensors can produce more accurate estimates of instantaneous rain rate, orbital characteristics mean these are not available over the entire globe simultaneously at a single instant in time.

Todd and Washington (1999) recently developed a method to reconstruct the GPI from cloud-top statistics contained in the International Satellite Cloud Climatology Project (ISCCP) D1 dataset. A long-term dataset, from 1983 onwards, of 3-hourly rainfall estimates on a 2.5° grid from 40°N–40°S, has subsequently been produced using this method. This data has proved to be a valuable resource for climate studies, particularly those concerned with global and regional rainfall variability at diurnal, synoptic, and intraseasonal timescales (Washington and Todd 1999).

Satellite IR algorithms benefit from the high temporal sampling of geostationary satellites, but IR radiances from cloud tops have only a weak, indirect relationship with surface rainfall. Therefore, many simple IR algorithms rely on the effects of scale averaging to improve accuracy. For example, the GPI (Arkin and Meisner 1987), one of the most widely used and thoroughly evaluated satellite rainfall estimation techniques, derives rainfall (R) over some large grid cell (e.g., 2.5°) from

$$R = F_c G T, \tag{1}$$

where F_c is the fractional coverage of each grid cell by cloud colder than the 235-K threshold, G is the GPI coefficient equal to 3.0, and T is the number of hours in the integration period.

This is based on the observations of Richards and Arkin (1981) that rainfall is strongly correlated with fractional coverage of cold cloud (less than 235 K) when averaged over some large area or time. Atlas and Bell (1992) show that the GPI is essentially an area–time integral (ATI) approach to rainfall estimation. The ATI approach has been used to estimate the storm rainfall volume from the area and duration of the storm, derived from radar data (Doneaud et al. 1984). The GPI uses cold cloud area as a surrogate for rain area. Thus, Atlas and Bell (1992) show that, in effect, the G coefficient can be defined as

$$G = R_c \left(\frac{A_c}{A_r} \right)^{-1}, \tag{2}$$

where R_c is the climatological conditional rain rate, and A_c and A_r are the average areas of cold cloud and rain, respectively, over the estimate sample space and time domains. The G coefficient reaches stable values for large timespace and/or scales because

1) the sample R_c over the estimate domain, and thus the probability density function of rainfall, approximate the true climatological population quantities, and
2) the sample ratio of A_c/A_r over the estimate domain is similarly representative of the typical storm structure for that climatic regime.

As long as the GPI is calculated over a large enough domain these conditions can often be satisfied. Richards and Arkin (1981) found that this is true for grid cells of 2.5° for periods as short as 1 h. At small scales these conditions are unlikely to be satisfied. In addition, it has been recognized that since R_c and A_c/A_r vary over space and time it is unlikely that a single G value or IR threshold will be appropriate for all regions (Arkin et al. 1994). This suggests that both G and IR thresholds should be sensitive to broad-scale variation in the dominant cloud microphysical processes. Todd et al. (1995, 1999) showed that optimum IR threshold values (calculated by comparison to rain gauges) over East Africa are highly variable in time and space, as a result of local-scale rainfall/cloud characteristics, often associated with orographic rainfall processes. Such optimized IR threshold fields were shown to identify rainfall events more accurately than a fixed 235-K threshold. Xu et al. (1999) demonstrated the value of local calibration of IR thresholds and G (using PMW satellite on a monthly basis) over the Japanese Islands and surrounding seas, while Huffman et al. (2001) demonstrate a similar algorithm for global rainfall estimates.

In this paper we describe a new combined PMW/IR microwave/infrared rainfall algorithm (MIRA) for estimation of small-scale rainfall (down to the instantaneous/pixel scale) that addresses the primary limitations of the GPI. In section 2 we describe the nature and sources of the PMW and IR satellite data and indepen-

TABLE 1. Details of the data used in this study.

Data type	Period	Region
Geostationary satellite IR (GMS)	Nov 1992–Feb 1993	TOGA COARE (4°N–1°S, 153°–158°E)
Geostationary satellite IR (Meteosat, GMS, GOES-E, GOES-W)	Jul 1991, Jul 1992, Jan 1993	Global (40°N–40°S)
Satellite PMW (DMSP *F11* SSM/I)	Nov 1992–Dec 1993	TOGA COARE (4°N–1°S, 153°–158°E)
Satellite PMW (DMSP *F11* SSM/I)	Jul 1992, Jan 1993	Global (40°N–40°S)
Satellite PMW (DMSP *F10* SSM/I)	Jul 1991, Jul 1992	Global (40°N–40°S)
TOGA COARE shipborne radar	Nov 1992–Feb 1993	TOGA COARE (4°N–1°S, 153°–158°E)
High-density EPSAT daily rain gauge data	Jul 1992	13°–14°N, 2°–3°E
GPCP pentad rain gauge data	Jul 1991	Selected 2.5° grid cells (see Table 2)
WetNet PIP-3, GPCC, and CPRD monthly rain gauge data	Jul 1992 and Jan 1993	Selected 2.5° grid cells (see Morrissey et al. 1994)

dent validation data used in the study. Section 3 provides a description of the MIRA algorithm and illustration of some ''global'' (40°N–40°S) products, while section 4 provides the results of an extensive validation, conducted over a range of time– and space scales relating to the wide range of potential applications.

2. Data and methods for evaluation of the MIRA algorithm

a. Satellite data

Two sets of IR data were utilized. Hourly, full-resolution IR imagery from the Geostationary Meteorological Satellite were obtained for the Tropical Ocean Global Atmosphere Coupled Ocean–Atmosphere Response Experiment (TOGA COARE) region of the Pacific (4°N–1°S, 153°–158°E) for the period listed in Table 1. Second, in order that the MIRA algorithm could be developed and tested over an extended period and area suitable for large-scale climate applications, satellite IR data were obtained from the ISCCP in the form of the DX dataset (Table 1). This dataset contains global satellite IR radiances subsampled to a 30-km grid and a 3-hourly interval (Rossow and Schiffer 1991).

Global PMW data from the Special Sensor Microwave Imager (SSM/I) on board the Defense Meteorological Satellite Program (DMSP *F10* and *F11*) satellites were obtained for the same periods as the IR data (Table 1). SSM/I data are available from 1987 to present and so represent the most appropriate source of PMW data currently available for most climate studies.

b. Independent validation data

Validating satellite estimates of rainfall is notoriously problematic, not least because of the difficulty in obtaining accurate independent estimates of rainfall with similar spatial and temporal characteristics to those of the satellite quantity. In this study we invoke a number of procedures to provide a validation of the MIRA algorithm that is as thorough as possible. Using the data described below (summarized in Table 1), MIRA estimates are validated over a range of scales, from instantaneous estimates at 12 km to monthly estimates at 2.5°.

1) INSTANTANEOUS ESTIMATES OF RAIN RATE FROM THE AIP-3 TOGA COARE RADAR

Within the Algorithm Intercomparison Project (AIP) TOGA COARE study region a number of ship study cruises were conducted in which shipborne radar systems were operated [full details can be found in Ebert and Manton (1998)]. For this study only, data points within 100 km of the radar were used, and the original 2-km data were binned to a 12-km grid to match the minimum resolution of the SSM/I sensor.

2) INSTANTANEOUS RAIN-RATE ESTIMATES FROM SSM/I DATA

Estimates of rain rate from combined PMW/IR methods were compared with estimates from the PMW alone at a range of spatial scales, from 0.25° (approximating the ISCCP DX IR pixel size) to 2.5°. A jackknife procedure was invoked to ensure validation data independence. In this procedure, a collection of calibration datasets was constructed, each of which composed the full calibration set with a single day's data removed. This enables a more spatially extensive validation (over the region 20°N–20°S, 140°E–180°) than that afforded by the TOGA COARE radar data.

3) DAILY RAIN GAUGE ESTIMATES

Under the Hydrological and Atmospheric Pilot Experiment in the Sahel (HAPEX-Sahel) project, the EPSAT network of rain gauges was established. A total of 107 rain gauges was installed within a single $1° \times 1°$ cell, centered on 13.5°N, 2.5°E, providing daily rainfall estimates for 1992–93 (Lebel and Amani 1999). From this, spatially averaged rainfall estimates were constructed using a simple spatial averaging technique. This dataset provides accurate estimates of daily rainfall at the same spatial scale as the highest-resolution satellite

TABLE 2. Grid cell locations of the GPCP pentad rain gauge data product.

Country	Grid cell longitude	Grid cell latitude	Number of gauges
Australia	130	−17.5	14
Australia	132.5	−17.5	10
Australia	130	−15	49
Australia	132.5	−15	8
Honduras	272.5	12.5	15
Honduras	272.5	15	4
Israel	35	32.5	1
Israel	32.5	30	3
Puerto Rico	292.5	17.5	62
Thailand	102.5	15	90

global climate rainfall estimates currently available (GEWEX 1996).

4) PENTAD RAIN GAUGE ESTIMATES

Estimates of pentad rainfall from rain gauges have been produced by the Global Precipitation Climatology Project (GPCP) on an experimental basis. The data cover a range of locations across the globe (Table 2) at a spatial resolution of 2.5°. We believe this data is the most spatially extensive gridded gauge dataset available for periods shorter than 1 month. However, the accuracy of these estimates is known to be compromised by inconsistent gauge observation times and an interpolation method not fully evaluated for short period estimates (A. McNab 1999, personal communication).

5) MONTHLY RAIN GAUGE ESTIMATES

A comprehensive set of monthly rainfall data for many parts of the globe (binned to a 2.5° grid) was prepared for the National Aeronautics and Space Administration (NASA) WetNet 3rd Precipitation Intercomparsion Project (PIP-3). This includes estimates over a variety of land regions [from the Global Precipitation Climatology Center (GPCC)] and Pacific atolls [from the Comprehensive Pacific Rainfall Database (CPRD)] to represent oceanic rainfall (Morrissey et al. 1994).

c. Statistical methods

Here we use the standard statistics of mean bias, correlation coefficient (CC), and root-mean-square error (rmse) to assess the quantitative accuracy of satellite estimates, and the area-weighted classification error score (AWES) of Todd et al. (1995) to asses the estimate of rain area. To account for the general condition that rainfall constitutes only a minority of observation points, the AWES weights errors of omission by the area of rain and areas of commission by the area of no rain:

$$\mathrm{AWES} = \frac{N_r}{R_r + N_r} + \frac{R_n}{N_n + R_n}, \tag{3}$$

where the upper (lower) case refers to the satellite (independent validation) quantity, such that R_r represents independent rain observations correctly classified by the satellite method, R_n independent nonrain observations incorrectly classified by satellite, N_n correctly classified nonrain observations, and N_r independent rain observations incorrectly classified as no rain. A perfect classification (misclassification) produces an AWES of 0.0 (2.0).

3. Principles and illustration of a new satellite passive combined microwave/infrared rainfall algorithm (MIRA)

Combined PMW and IR algorithms have been developed in the past, many of which represent developments of the GPI. Adler et al. (1993) developed the adjusted GPI (AGPI), in which a correction factor is derived from comparison of PMW and GPI estimates for coincident time slots over some extended period (e.g., 1 month). This correction is then retrospectively applied to all the hourly GPI estimates during that period. The AGPI is used routinely in the GPCP global monthly merged rainfall product (Huffman et al. 1997). Kummerow and Giglio (1995) and Xu et al. (1999) have subsequently developed a more sophisticated approach [termed by the latter the Universally Adjusted GPI (UAGPI) method], in which both the monthly IR threshold and G are optimized using coincident PMW and IR data, again over an extended period. Anagnostou et al. (1999) present a PMW-calibrated IR method for regional-scale applications.

Here we present MIRA, a new combined PMW and IR satellite algorithm for estimation of rainfall at the smallest possible time-space and scales. It is based on the assumption that PMW algorithms can provide accurate estimates of instantaneous rain rates and that this information can be used to calibrate IR parameters, to improve rainfall estimates from IR data at high temporal frequency. It is widely accepted that satellite-borne microwave sensors provide the most accurate estimates of rain rate currently available at quasi-global scales. In the form presented here, we use PMW estimates of rain rate, although the algorithm can utilize data from satellite-borne precipitation radar just as readily.

The frequency distributions of PMW-estimated rainrate (R_{MW}) and IR brightness temperature ($\mathrm{IR}_{\mathrm{Tb}}$) values are derived from *coincident* satellite imagery, accumulated over some space and/or time domain large enough to ensure sufficient IR and PMW observations. This domain is hereafter referred to as the calibration domain. To derive an optimized $\mathrm{IR}_{\mathrm{Tb}}$–rain rate relationship for that calibration domain, the Probability Matching Method (PMM) of Atlas et al. (1990) is used. In the PMM the histograms of coincident R_{MW} and $\mathrm{IR}_{\mathrm{Tb}}$ observations are compared, such that the proportion of

the R_{MW} distribution above a given rain rate is equal to the proportion of the IR_{Tb} distribution below the associated IR_{Tb} threshold value. Working from the highest to lowest rain rates, by calculating the proportion of the R_{MW} distribution above rain rates at some small interval (0.1 mm h^{-1}) the appropriate IR_{Tb} threshold values are derived. In this way an ''optimized'' IR_{Tb}–rain rate relationship is produced. The method ensures that

$$A_{c(t)} = A_{r(R)}, \tag{4}$$

where R is a given PMW rain rate and t is the associated IR_{Tb} threshold. The IR_{Tb} threshold that equates to the lowest measurable PMW rain rate (0.1 mm h^{-1}, in the case of the PMW algorithms presented here) represents the optimum IR rain/no-rain threshold ($IR_{Tb(T)}$), equivalent to the quantities derived by comparisons of IR and rain gauge data by Todd et al. (1995, 1999).

In this method the physically sensible assumption is made that low (high) IR_{Tb} values are most likely to be associated with higher (lower) rain rates. It has long been known that there exists only a weak statistical relationship between IR_{Tb} and rain rate. In this case, however, the relationship is derived only for the particular calibration domain and is therefore variable over space and time, providing sensitivity to actual variations in cloud and rainfall relationships. The optimized IR_{Tb}–rain rate relationships resulting from the PMM procedure can then be applied to IR images to derive instantaneous rain-rate estimates at the high frequency of a geostationary IR sensor. Through the application of spatially and temporally variable optimized IR_{Tb}–rain rate relationships the limitations in existing IR-only methods identified in section 1 are addressed. Although estimates are made at the temporal resolution of the geostationary IR imagery, accuracy is limited by the ability of the PMW algorithm to estimate the true probability density function of rainfall.

Further, PMW calibration cannot counter all the limitations of IR data. There will remain occurrences of nonraining cloud that is colder than the optimum IR threshold, and raining cloud that is warmer than the IR threshold. Within rain systems vertical wind shear can be an important source of such problems. Clearly the smaller the dimensions of the calibration domain the greater will be the sensitivity to such conditions. At larger scales, compatible with climate products, the calibration is designed to respond to systematic variations in cloud–rainfall relationships, for example, to identify areas of persistent nonraining cirrus such as the jet stream regions of the subtropics.

Setting the space/time dimensions of the MIRA calibration domain is, therefore, an important consideration. The only requirement is that the domain is large enough to ensure sufficient observations. However, a trade-off between the number of observations and sensitivity to local (in time and space) cloud microphysical variability is expected to exist. Section 4a deals specifically with this issue. In practice the most appropriate domain size is determined by the nature of the application. This study is concerned primarily with rainfall products to support climate analysis, and [for validation purposes (Section 4b)] a time dimension of 1 month and a spatial dimension ranging from 1° to 2.5° are used. Estimates at 0.25° are derived using a moving 1° neighborhood window to ensure sufficient observations.

MIRA optimum IR rain/no-rain thresholds ($IR_{Tb(T)}$) reflect the relationship of rainfall and cloud-top characteristics within the calibration domain. An analysis of their space/time structure is instructive because it provides not only an overview of the nature of the MIRA optimization process, but also an insight into rainfall processes. Figures 1 and 2 present fields of MIRA $IR_{Tb(T)}$ and monthly rainfall derived over the global Tropics and subtropics, with a 1° per 1 month calibration domain, using the PMW Bristol University Combined (BUC) algorithm (Smith et al. 1998). The rationale for the use of the BUC algorithm is provided in section 4b.

An important finding here is that values of $IR_{Tb(T)}$ vary substantially over space and time. During July 1992 and January 1993, variations reflecting the planetary-scale circulation are apparent (Figs. 1 and 2). A broad distinction is apparent between low thresholds (200–240 K) associated with regions of high rainfall (Fig. 2a), notably in the tropical concergence zones and the humid midlatitude regions, and higher thresholds (260–290 K) over the dry regions of the subtropical high-pressure zones and dry season Tropics. This reflects the existence of persistent cold cloud during wet season conditions, which necessitates generally low-threshold values to exclude nonraining cloud.

There is also substantial and important regional variability suggesting that there is no consistent relationship between $IR_{Tb(T)}$ and rainfall amount. Figure 3a presents a transect of rainfall and $IR_{Tb(T)}$ values averaged over the latitude band 5°–15°N (broadly corresponding to the ITCZ region) during July 1992. Values are lowest (210–230 K) where rainfall maxima occur, over south Asia and the Indian Ocean (70°–100°E). These are the regions of persistent, intense convection, resulting in IR_{Tb} distributions dominated by low values. Higher $IR_{Tb(T)}$ values (around 230 K) occur over tropical West Africa (10°W–30°E) and the Maritime Continent. $IR_{Tb(T)}$ are higher still (240–255 K) from the western and central equatorial Pacific toward the date line. In the eastern equatorial Pacific (160°E–120°W) and the equatorial Atlantic Ocean (20°–60°W), thresholds reach a peak of around 260–270 K. In both these regions monthly rainfall exceeds 200 mm. It is interesting to note, therefore, that there are extensive regions throughout the Pacific and Atlantic Oceans where rainfall is extensive but appears to be associated with relatively warm-topped cloud. This is in line with the findings of Petty (1999), which were based on a comparison of IR imagery and Comprehensive Ocean–Atmosphere Data Set (COADS) reports of rainfall. The variability in cloud and rainfall characteristics along the ITCZ is highlighted by a com-

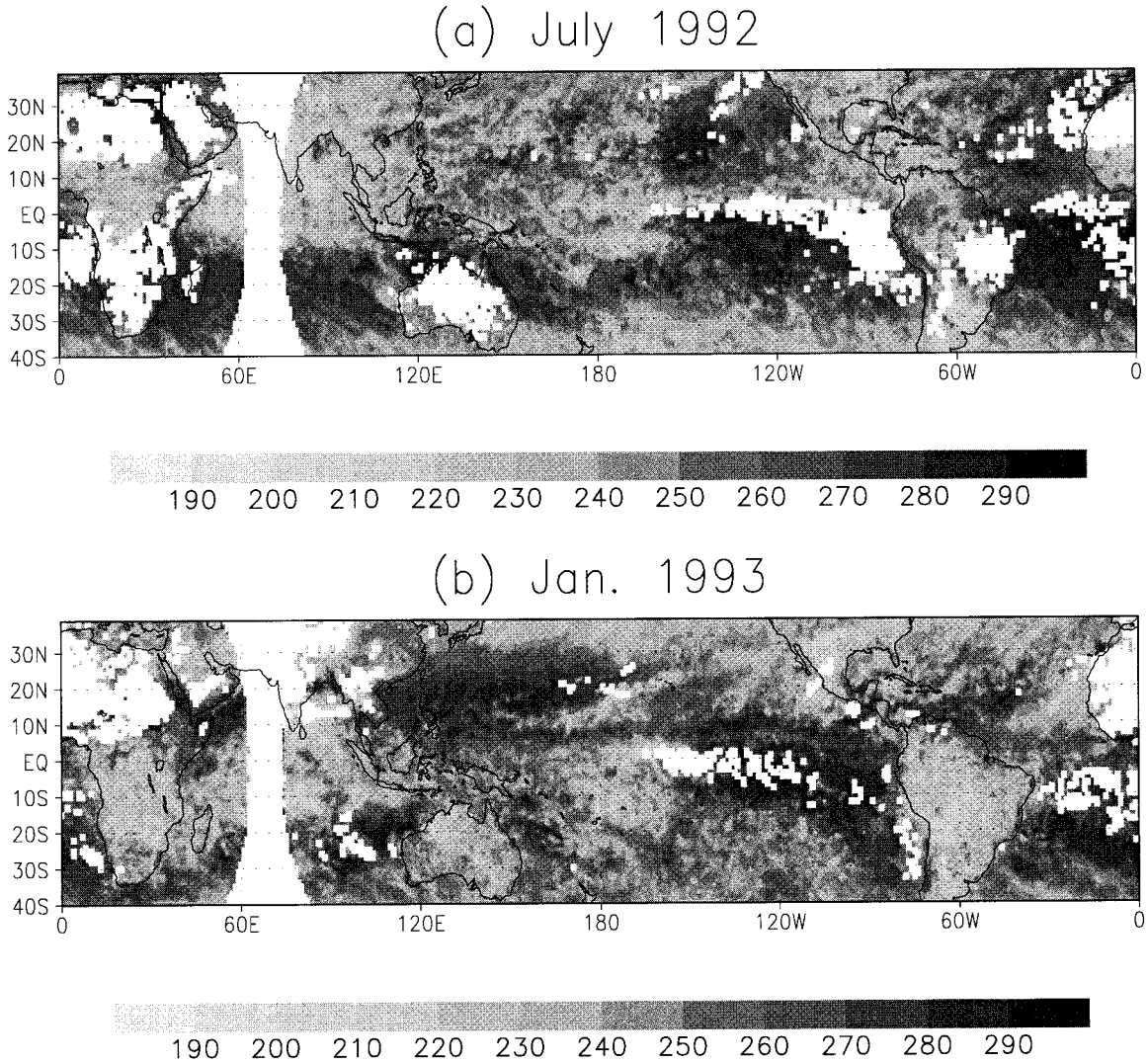

FIG. 1. $MIRA_{[BUC]}$ optimum IR rain/no-rain threshold temperatures (K) for (a) Jul 1992 and (b) Jan 1993, calculated using a 1° per 1 month calibration domain.

parison of thresholds over northern South America (~225 K) and the adjacent Pacific (~235 K) and Atlantic (~265 K) Oceans.

Pronounced variability at the local scale is also apparent in some regions. For example, along the southern coast of West Africa thresholds are high, exceeding 260 K, despite rainfall as high as neighboring inland regions, where thresholds are some 30 K lower. This may relate to the prevalence of persistent warm rain cloud noted by Dewhurst et al. (1996). Thresholds are locally high over the highlands of Ethiopia where orographic enhancement of rainfall is likely (Todd et al. 1995, 1999).

A similarly complex pattern emerges in January 1993 (Figs. 1b, 2b, and 3b). Low thresholds (~225 K) are observed over the major centers of continental convective rainfall (equatorial West Africa, southern Africa, Amazonian South America, and northern Australia). Over oceanic regions of the ITCZ (the equatorial Atlantic and the Maritime Continent) thresholds are higher (~255–265 K). Areas of exceptionally high thresholds (above 280 K) where rainfall is substantial (greater than 200 mm) include the ITCZ through the Pacific Ocean east of the Philippines (8°–10°N), and the Indian Ocean west of Australia (around 15°S). These regions appear to experience predominantly warm rainfall processes. In contrast, oceanic regions where high rainfall is accompanied by low threshold values (around 230 K) include the tropical equatorial Indian Ocean and the zonal section of the South Pacific convergence zone (SPCZ) at around 10°S, 180°. Along the diagonal portion of the SPCZ (to 30°S, 150°W) thresholds rise to 270 K, suggesting that a transition from deep convective systems to shallower convection in the subtropical zone occurs.

MIRA-optimized IR_{Tb}–rain rate relationships are presented in Fig. 4 for five 1° grid cells at selected locations along the ITCZ and the SPCZ, during July 1992. The

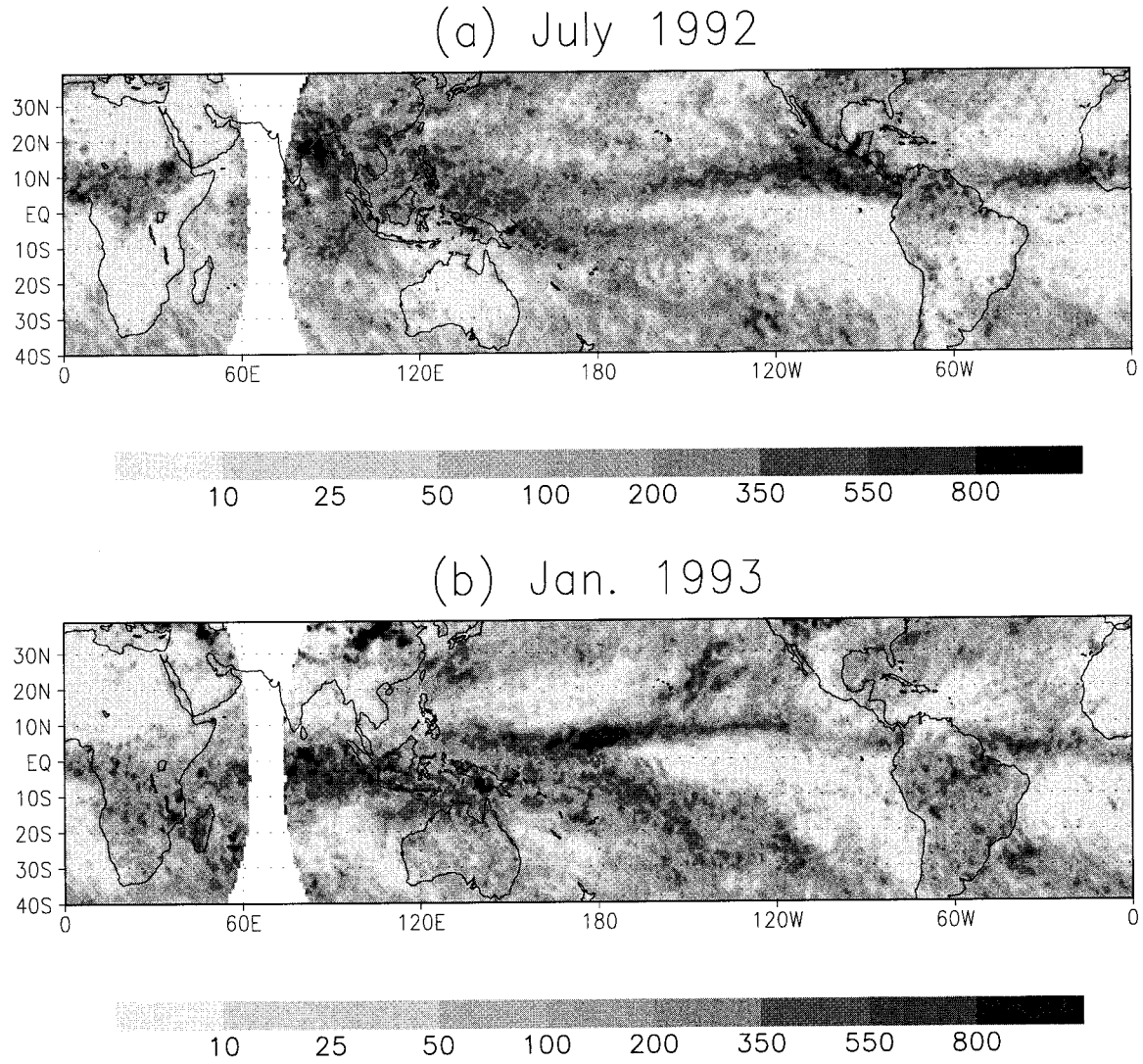

FIG. 2. $MIRA_{[BUC]}$ rainfall estimate (mm) for (a) Jul 1992 and (b) Jan 1993.

cells were selected to highlight variations in cloud and rainfall characteristics, and illustrate the pronounced variability in cloud characteristics observed in association with rainfall. Rainfall is associated with only cold cloud over the Indian, Sahelian, and SPCZ locations. In contrast, over the Atlantic and Pacific ITCZ locations the range of IR cloud temperatures associated with rainfall is far larger, such that in the latter case cold and relatively warm rain processes are indicated. Of particular note is the ''warm'' rain over the Atlantic ITCZ region where an $IR_{Tb(T)}$ of 270 K is observed.

The $IR_{Tb(T)}$ and the IR_{Tb}–rain rate relationship calculated within MIRA, illustrated above, reflect variations in cloud and rainfall microphysical processes, which results in pronounced spatial and temporal variations in the relationship of cloud-top characteristics and rain rate. This provides compelling evidence for the likely value of locally calibrating an IR method.

4. MIRA validation

a. Sensitivity to calibration domain size

As described in section 1, the principal aim of MIRA and similar algorithms is to account for variability in cloud and rainfall processes. Such variability is likely to occur at a range of temporal scales, from diurnal, through intraseasonal, to seasonal and interannual. Spatial variations occur over a similarly wide range of scales, with small-scale variability pronounced over rapidly varying surface types, such as mountainous terrain and coasts. Rainfall is often characterized by sparse and short-lived events, with intensities heavily biased towards lower rain rates. Thus the calibration domain must be large enough to represent the infrequent higher rain rates but small enough to provide sensitivity to cloud microphysical variations in space and time.

The sensitivity of MIRA to the size of the calibration

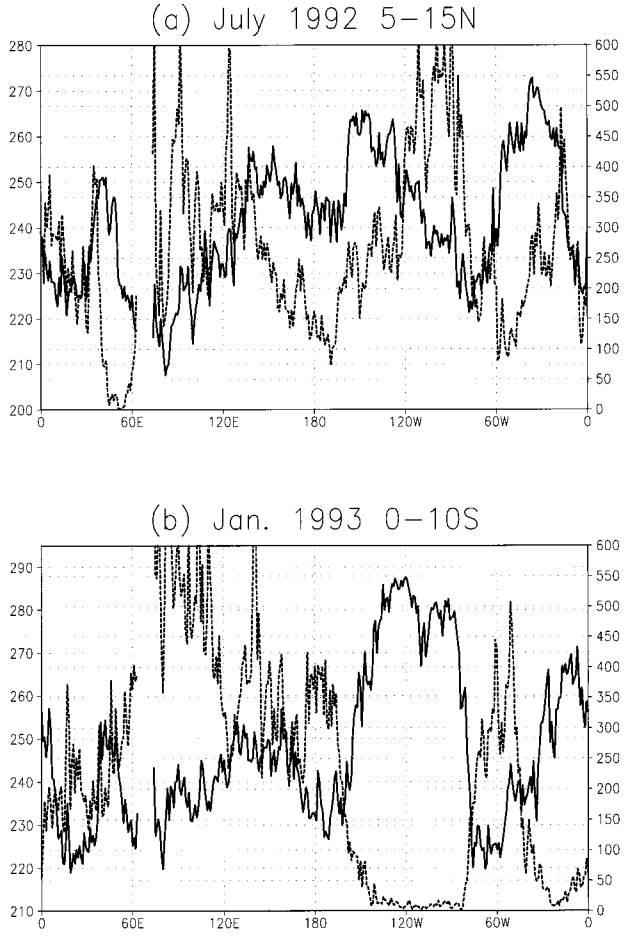

FIG. 3. Longitude transect of $MIRA_{[BUC]}$ optimum IR thresholds [solid line, left-hand scale (K)] and rainfall [dashed line, right-hand scale (mm)], averaged between latitudes (a) 5°–15°N in Jul 1992 and (b) 0°–10°S in Jan 1993.

domain is assessed by comparing MIRA estimates of instantaneous rain rate, derived using a range of calibration domain dimensions, with independent AIP-3 TOGA COARE radar data. All estimates have a spatial resolution of 12 km. The use of coincident IR, PMW, and radar data from the TOGA COARE region means that the spatial domain of the data is relatively small (all points lie within 100 km of the ship radar). In the analysis, the spatial dimension of the domain is held constant and the temporal dimension varies over periods of less than 1 min (a single SSM/I swath) to 4 months (all AIP TOGA COARE data). The major PMW rainfall algorithm used is the ''BA3'' algorithm, a simple empirically calibrated frequency difference algorithm utilizing the 19- and 85-GHz channels [see Ebert and Manton (1998) for full description]. Hereafter, all references to combined PMW/IR algorithms indicate the PMW algorithm used with a subscript, for example, $MIRA_{[BA3]}$. For comparison, we also present analysis of estimates from MIRA calibrated with the widely used National Oceanic and Atmospheric Administration (NOAA) Microwave Index (NMI) of Ferraro et al. (1996).

Table 3 shows the validation statistics of the $MIRA_{[BA3]}$ algorithm for three different calibration scenarios, where the IR_{Tb}–rain rate relationships are generated by the PMM method using (i) all the data available (approximately 4 months); (ii) each ship cruise (approximately 1 month); (iii) each individual case of a coincident SSM/I swath/IR image; and (iv) as (iii) but only where a minimum number of 250 rain points are observed in the domain, otherwise the nearest (in time) calibration relationship is used. The validation results apply to MIRA estimates at the time of the SSM/I swath, such that the accuracy results generated under (iii) and (iv) may not apply to times between calibration periods. For comparison, the statistics are presented for the PMW BA3 algorithm and the IR-only GPI.

Utilizing the smallest possible temporal domain (a single coincident SSM/I swath and IR image) results in an improved correlation in comparison to longer calibration periods. This demonstrates the benefit of utilizing a calibration domain that is as small as possible to maximize the accuracy of MIRA estimates. The results suggest that rainfall variability at diurnal, synoptic, and intraseasonal timescales all introduce variability in cloud microphysics, which results in lower correlation coefficients for longer calibration periods. The minimum number of points appears less important in the calibration process than proximity in time. This result is likely to have implications for applications such as initialization of NWP models. It is interesting to note that the bias, ratio, and rmse remain relatively constant, irrespective of the calibration domain period, as they are determined largely by the performance of the PMW algorithm. There are factor of 2 differences between the AIP-3 ship radar and $MIRA_{[BA3]}$ estimates, just as there are with the BA3 algorithm, and indeed many of the SSM/I algorithms evaluated in AIP-3 (Ebert and Manton 1998). For this study, however, these statistics are less interesting than the CC and AWES, which represent the ability of the algorithm to accurately replicate variability in rainfall. In this regard, MIRA provides a substantial improvement in estimate accuracy at these small scales relative to the GPI, irrespective of the calibration domain period used. Table 4 shows the correlation coefficients of instantaneous rain rates from the PMW SSM/I, the GPI, and MIRA, with radar at a range of spatial scales. The improvement of MIRA over the GPI is most pronounced at the smallest spatial scales (and, by implication, at the smallest temporal scales).

These results indicate that MIRA can produce useful estimates of rain rate at the smallest possible scales, with a CC roughly midway between the PMW algorithm and the GPI. Thus, we are able to specify the expected accuracy of MIRA estimates in terms of the parent PMW algorithm. Clearly PMW-calibrated IR methods are sensitive to the accuracy of the PMW algorithm. Previous intercomparison projects have shown that PMW satellite

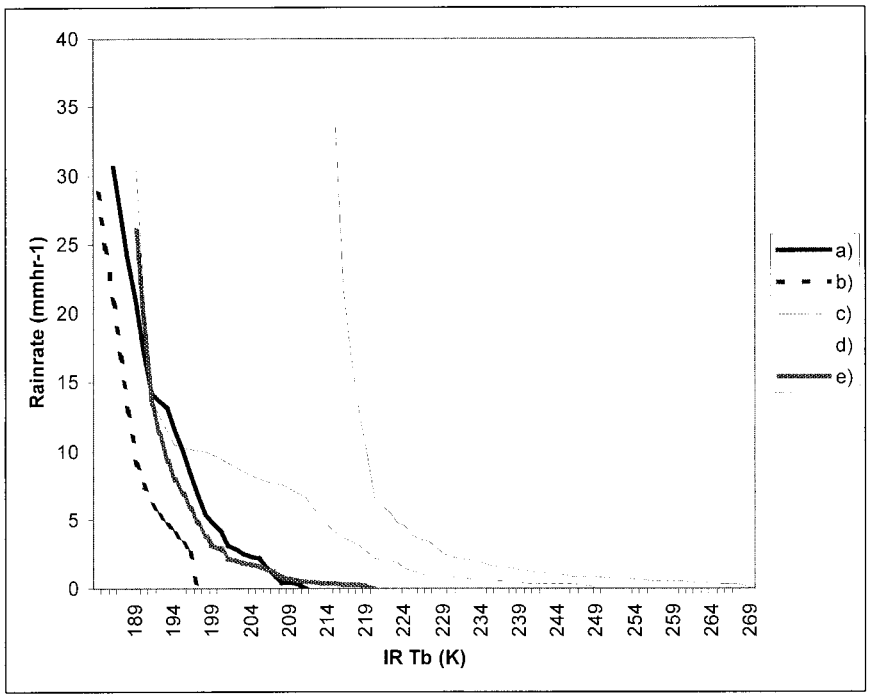

FIG. 4. $MIRA_{[BUC]}$ IR_{Tb}–rain rate relationships for selected locations during Jul 1992, calculated using a 1° per 1 month calibration domain. The coordinates of the bottom left corner of each cell are (a) 13°N, 2°E (EPSAT, Niger); (b) 23°N, 87°E (Bengal, India); (c) 8°N, 31°W (central Atlantic); (d) 12°N, 142°W (east Pacific); and (e) 7°S, 174°W (SPCZ).

algorithms can differ widely in their accuracy. In this context, it is interesting to note that the correlation of rain rate estimated by empirical PMW algorithms (BA3 and NMI) and radar is high, considering the small time- and space scales, which generally encourages confidence in both PMW methods and MIRA. It may be expected that MIRA will produce greater improvements in accuracy in comparison to the GPI over land regions where the GPI is known to substantially overestimate rainfall.

b. Validation of MIRA estimates over the global Tropics and subtropics

The results of section 4a show that MIRA estimates (at the time of SSM/I overpass) over the TOGA COARE region of the tropical Pacific are most accurate when the calibration domain is as small (in the time dimension) as possible. Such a condition is likely to apply in regions such as the tropical Pacific warm pool, where rainfall is consistently present even within small calibration domains. In regions where rainfall is more infrequent it is expected that a larger calibration domain is necessary to ensure sufficient rainfall observations from the infrequent PMW imagery. Therefore, for quasi-global applications we have used a gridded calibration domain of 1 month (which also has the effect of minimizing the impact of errors associated with bad satellite data) and a range of spatial dimensions ranging from 1° to 2.5°. Estimates are also derived at 0.25° in which a moving 1° calibration domain is used to ensure sufficient observations. Analysis of the 2.5° estimates is justified primarily because of the availability of extensive validation data at this scale. However, we provide a validation of the 2.5° estimates at smaller temporal scales than in many previous studies.

For quasi-global application the PMW BUC algorithm was selected for a number of reasons. The algorithm accounts for spatial and temporal variations in the PMW surface emission signal, and as such produces estimates over land, ocean, and coastal surfaces. Over oceans the algorithm identifies both a scattering and emission rainfall signal in the PMW data. This is of particular relevance given the importance of ''warm'' rain processes over the tropical Pacific, at least (Petty 1999). The results of PIP-3, the most extensive global algorithm validation exercise conducted to date, show that the BUC algorithm performed well, particularly in the tropical and subtropical regions (Kidd et al. 1998).

Table 5 presents the validation statistics of $MIRA_{[BUC]}$, GPI, and $UAGPI_{[BUC]}$ estimates at a wide range of spatial and temporal scales. Figure 5 presents scatterplots of $MIRA_{[BUC]}$ and $UAGPI_{[BUC]}$ estimates of instantaneous rain rate versus the independent SSM/I BUC estimates at a 0.25° spatial scale, approximating the ISCCP DX IR pixel size [see section 2b(2)]. $MIRA_{[BUC]}$ produces an encouragingly high correlation coefficient (0.47), and the improvement in estimation accuracy over the UAG-

TABLE 3. Statistics for $MIRA_{[BA3]}$, BA3, and GPI estimates of instantaneous rain rate (12-km resolution), under a range of calibration domain periods, compared with TOGA COARE radar.

Satellite algorithm	Bias (mm h^{-1})	Ratio	Rmse (mm h^{-1})	CC	*n*	Mean (mm h^{-1})	AWES
$MIRA_{[BA3]}$ (i) all data	0.25	1.99	1.84	0.25	53 121	0.51	0.61
$MIRA_{[BA3]}$ (ii) by cruise	0.25	1.99	1.82	0.27	53 121	0.51	0.61
$MIRA_{[BA3]}$ (iii) by case	0.25	1.97	1.75	0.32	53 121	0.51	0.49
$MIRA_{[BA3]}$ (iv) by case (>250 rain obs.)	0.27	2.03	1.8	0.28	53 121	0.52	0.55
GPI	0.21	1.82	1.72	0.20	53 121	0.47	0.66
SSM/I BA3	0.23	1.91	1.6	0.45	53 121	0.49	0.42

$PI_{[BUC]}$ is due to an ability to resolve the full range of rain rates, up to the maximum rain rate estimated by the PMW. In contrast, the UAGPI and GPI have rain rates equal to the mean PMW conditional rain rate and 3 mm h^{-1}, respectively. The skill exhibited by the GPI and UAGPI algorithms is derived from the identification of rain from no-rain conditions and, in the case of the UAGPI, from the spatial structure in the conditional rain rate field. Comparison with estimates at the 0.5° scale suggests that the limitations of this are more pronounced at the smaller spatial scales, in agreement with the results in Table 4. Previous studies have demonstrated only a weak relationship between IR_{Tb} and instantaneous rain rate. The results presented here suggest that locally calibrated IR_{Tb}'s contain useful information on rain rates, providing the potential for useful estimates at the pixel scale.

At the daily timescale (at 1° spatial resolution), $MIRA_{[BUC]}$ estimates again show a substantial (small) improvement in estimate accuracy in comparison to the GPI ($UAGPI_{[BUC]}$) (Table 5; Fig. 6). It is interesting to note that the correlation coefficient of 0.96 is exceptionally high for a satellite method, particularly at such small scales, and that the estimate bias is minimal. A time series of rainfall estimates from satellite and gauge is shown (Fig. 7), illustrating how $MIRA_{[BUC]}$ captures well the day-to-day variability in rainfall. That all the satellite methods produce impressive results in comparison with EPSAT data illustrates the value of independent gauge data with high gauge density, but may also reflect the limited spatial and temporal extent of this comparison. When estimates are integrated over the larger pentad/2.5° scale the results are more variable.

TABLE 4. Correlation coefficients satellite and TOGA COARE radar estimates of instantaneous rain rate.

	BA3	NMI	GPI	$MIRA_{[BA3]}$	$MIRA_{[NMI]}$
12 km	0.45	0.45	0.20	0.32	0.30
0.5° × 0.5°	0.60	0.59	0.32	0.43	0.38
1.5° × 1.5°	0.81	0.84	0.61	0.68	0.68

$MIRA_{[BUC]}$ and the $UAGPI_{[BUC]}$ show much-improved bias and rmse statistics in comparison with the GPI, which has a marked tendency to overestimate rainfall (Table 5; Fig. 8), demonstrating the value of some kind of PMW calibration of IR data. However, the GPI has a higher correlation with gauge rainfall. Validation at the monthly/2.5° scale is based on a much more comprehensive validation dataset (Table 5; Figs. 9 and 10). Here $MIRA_{[BUC]}$ and $UAGPI_{[BUC]}$ produce statistics in line with the BUC parent PMW algorithm. The GPI performs less well with a pronounced positive bias over land and a substantially higher (lower) rmse (correlation coefficient). Thus, it appears that there is little difference in the performance of MIRA, UAGPI, and the parent PMW algorithms for estimates averaged over large scales.

5. Summary and conclusions

In this paper we have outlined the major problems of estimating rainfall at small scales from satellite data, namely the inadequate temporal sampling of current microwave sensors and the indirect relationship between IR cloud-top characteristics and rainfall. However, demand from the climate and hydrological communities, for accurate rainfall estimates at such scales and over extended periods and areas, is growing. In this context we have introduced the MIRA algorithm, which combines PMW estimates of instantaneous rain rate with frequent IR imagery to account for limitations in each data source. The MIRA algorithm uses coincident PMW and IR observations over a spatially and temporally variable calibration domain to optimize the IR–rain rate relationship using a probability matching method.

The space/time dimensions of the calibration domain are shown to be important to the success of MIRA and other combined IR/PMW schemes, as is the choice of the PMW algorithm. Results show that over the tropical Pacific region MIRA estimates of instantaneous rain rate are most accurate when the calibration domain covers the shortest possible period. This suggests that the IR_{Tb}–

TABLE 5. Validation statistics of rainfall estimates from $MIRA_{[BUC]}$, $UAGPI_{[BUC]}$, and GPI.

Independent validation data	$MIRA_{[BUC]}$			$UAGPI_{[BUC]}$			GPI		
	CC	Ratio	RMSE	CC	Ratio	RMSE	CC	Ratio	RMSE
SSM/I BUC[a]	0.47	1.1	2.2	0.34	1.07	2.0	0.04	1.54	2.84
SSM/I BUC[b]	0.54	1.01	2.02	0.46	1.06	1.92	0.24	1.97	1.98
EPSAT gauge data[c]	0.96	1.08	2.04	0.89	1.04	2.44	0.76	1.4	5.3
GPCP gauge data[d]	0.54	1.76	25.17	0.51	2.01	29.7	0.66	2.74	36.9
WetNet PIP-3 GPCP land-based gauges[e]	0.8	1.24	82.6	0.81	1.24	70.6	0.69	1.69	147.5
WetNet PIP-3 Comprehensive Pacific Rainfall Database[f]	0.85	0.96	74.6	0.86	0.95	63.6	0.75	1.08	100.8

[a] 20°S–20°N, 140°E–180°, Jul 1991, 0.25°, conditional instantaneous, $n = 515$, mean = 1.7 mm h^{-1}.
[b] 20°S–20°N, 140°E–180°, Jul 1991, 0.5°, conditional instantaneous, $n = 228$, mean = 1.04 mm h^{-1}.
[c] 13°–14°N, 2°–3°E, Jul 1992, 1°, daily, $n = 30$, mean = 3.5 mm day^{-1}.
[d] Selected locations (Table 2), Jul 1991, 2.5°, pentad, $n = 46$, mean = 8.7 mm $pentad^{-1}$.
[e] Selected locations (see Morrissey et al. 1994), 2.5°, monthly, $n = 159$, mean = 83.7 mm.
[f] Selected locations (see Morrissey et al. 1994), 2.5°, monthly, $n = 17$, mean = 217.6 mm.

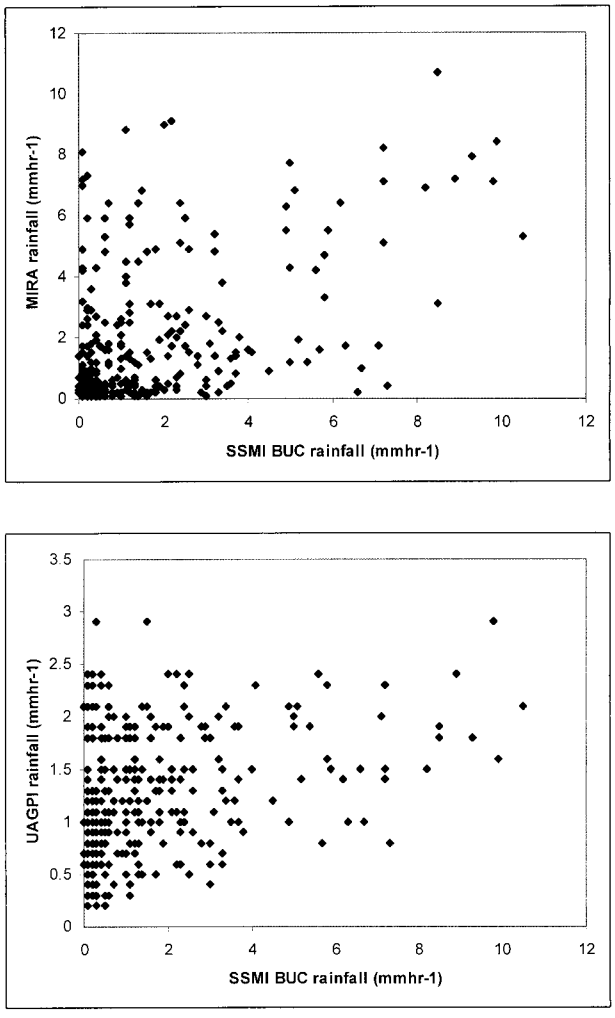

FIG. 5. Instantaneous rain rate (mm h^{-1}) at 0.25° resolution estimated using SSM/I BUC, $MIRA_{[BUC]}$, and $UAGPI_{[BUC]}$ over the tropical Pacific (40°N–40°S, 120°E–180°), where IR slots are within 10 min of the SSM/I pass.

rain rate relationship exhibits substantial variability at subdaily scales and beyond, at least in the AIP-3 TOGA COARE region.

The validation results point to two further principle conclusions. First, MIRA and the UAGPI exhibit substantial improvements in rainfall estimate accuracy compared to the GPI at all scales down to that of the satellite pixel. This clearly demonstrates the value of PMW calibration of IR parameters for both regional and quasi-global applications, and that improved estimates are possible at all scales. Thus, spatial and temporal variability in cloud microphysical processes can be better represented through local calibration of IR parameters. Second, the probability matching method by which MIRA is calibrated can provide useful improvements in estimate accuracy compared to the UAGPI (and GPI) at smaller scales (less than 2.5° per pentad). This suggests that IR_{Tb}'s contain sufficient information on rainfall to justify the application of a variable IR_{Tb}–rain rate relationship rather than simply the mean conditional rain rate, at least in the context of a locally variable calibration. This offers the prospect of improved estimates of instantaneous rain rate down to the scale of indvidual IR pixels. In relation to instantaneous estimates of rain rate from shipborne radar, MIRA estimate accuracy is roughly midway between the parent PMW algorithm and the GPI. When estimates are integrated over large areas (2.5° per pentad) the UAGPI and MIRA performances are comparable, suggesting that the fractional coverage of cloud below the optimum IR threshold is a very useful indicator of area-averaged rainfall.

However, estimates based on information from a single thermal IR channel are always likely to suffer from misclassification on nonraining ''cold'' cloud and raining ''warm'' cloud. The MIRA calibration procedure provides the ''optimum'' IR–rain rate relationship over the calibration domain area and period, which reduces misclassification errors. It is for this reason that MIRA estimate accuracy improves relative to the GPI with decreasing calibration domain size.

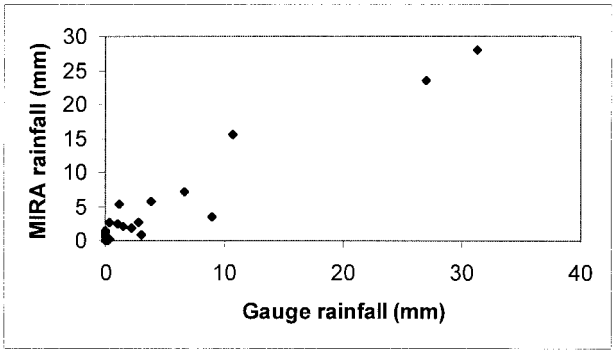

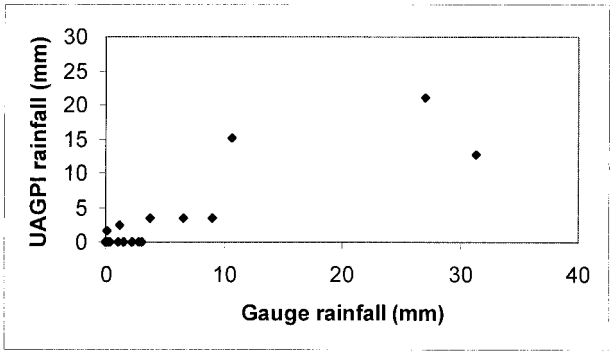

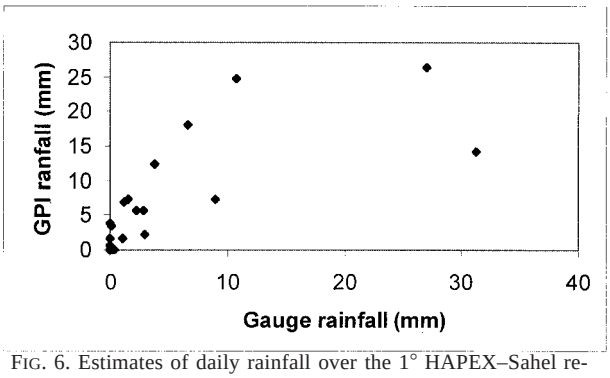

FIG. 6. Estimates of daily rainfall over the 1° HAPEX–Sahel region, from EPSAT rain gauges, $MIRA_{[BUC]}$, $UAGPI_{[BUC]}$, and GPI.

In the form presented here MIRA can be applied to long term datasets of satellite IR observations from the ISCCP DX products and SSM/I PMW data to produce a database of 3-hourly rainfall estimates on a 30-km grid over the global Tropics and subtropics, from 1987 to present. The final product would represent the most comprehensive set of satellite rainfall observations available for much of the globe and would provide a valuable new resource for climate studies. More recently, a rolling archive of full-resolution global IR composite images has been made available by the NOAA Climate Prediction Center/National Center for Environmental Prediction/National Weather Service (ftp://ftp.ncep.noaa.gov/pub/precip/global_full_res_IR/README), providing the potential for routine MIRA

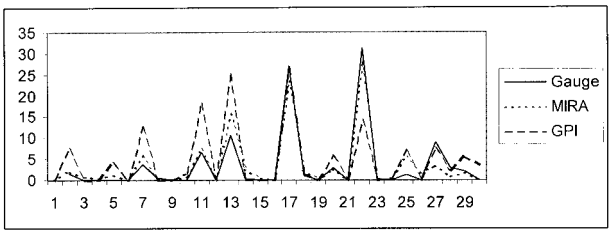

FIG. 7. Time series of daily rainfall over the 1° HAPEX–EPSAT region, from EPSAT rain gauges, $MIRA_{[BUC]}$, and GPI.

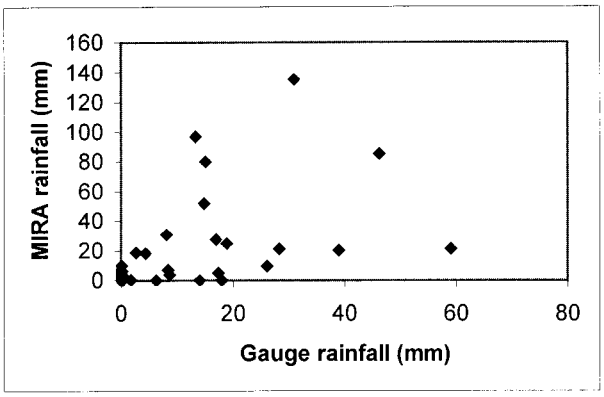

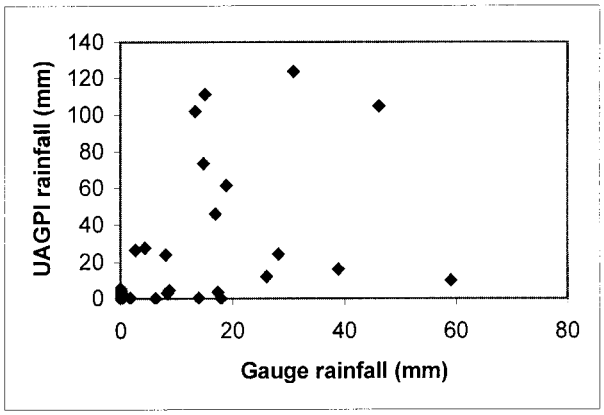

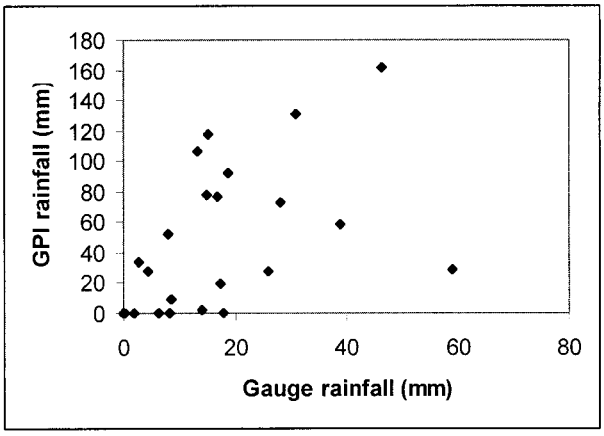

FIG. 8. Estimates of pentad rainfall over GPCP selected 2.5° land grid cells, from GPCP rain gauges, $MIRA_{[BUC]}$, $UAGPI_{[BUC]}$, and GPI.

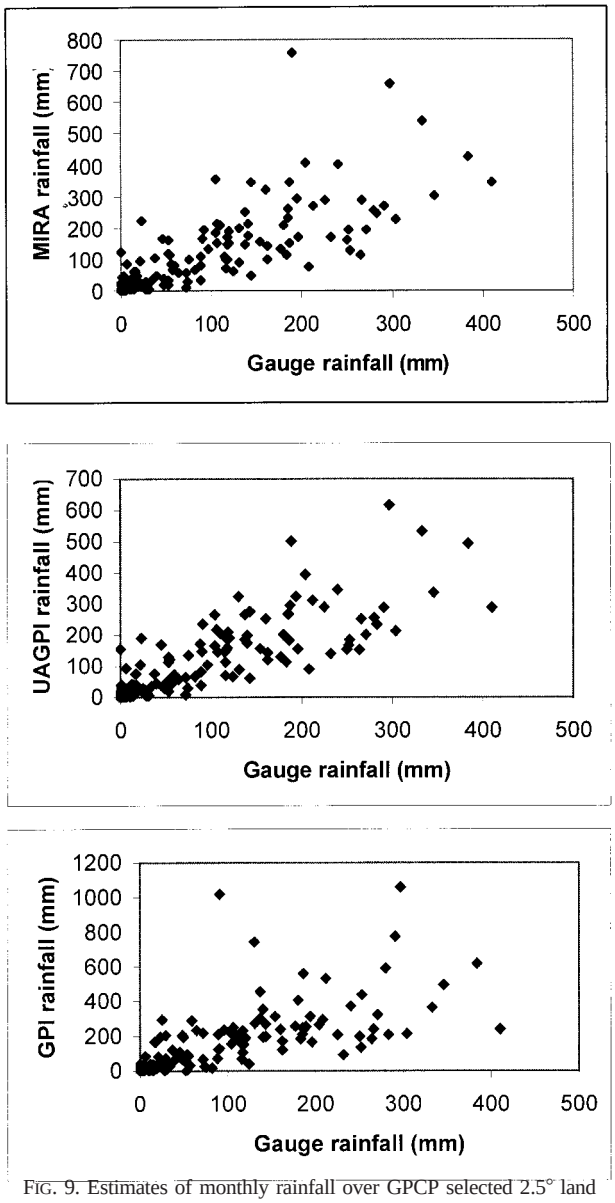

FIG. 9. Estimates of monthly rainfall over GPCP selected 2.5° land grid cells, from GPCP rain gauges, $MIRA_{[BUC]}$, $UAGPI_{[BUC]}$, and GPI.

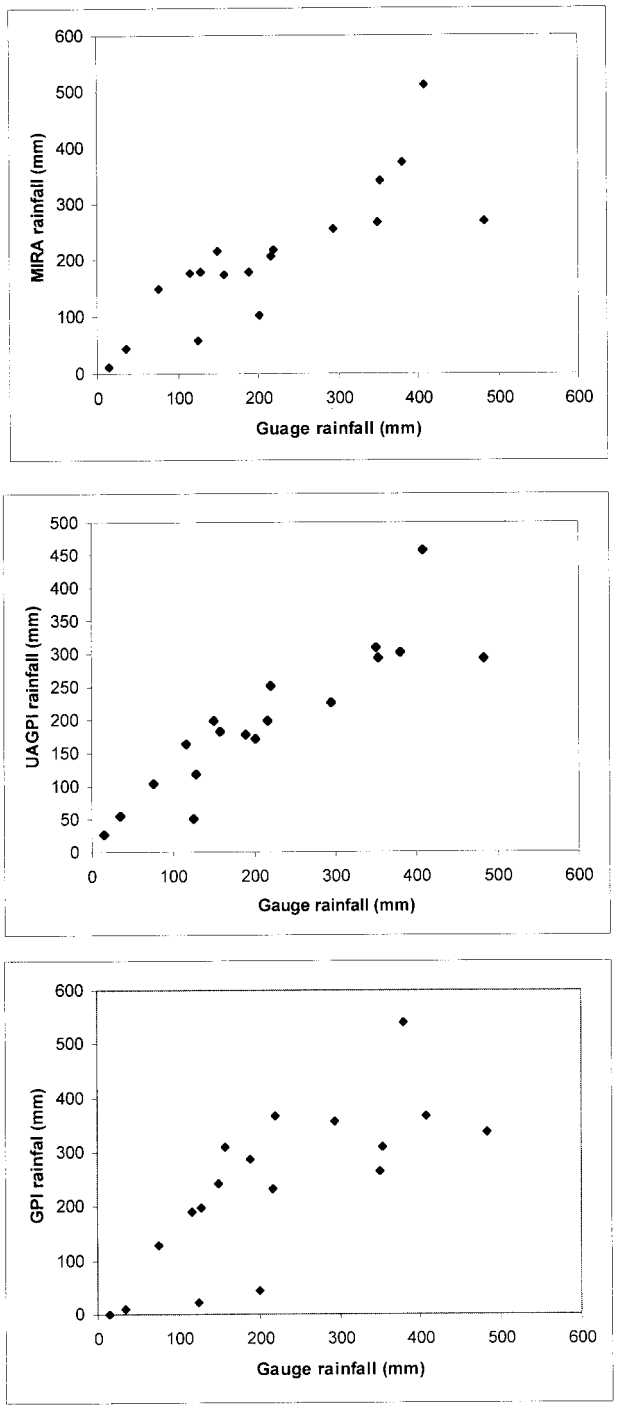

FIG. 10. Estimates of monthly rainfall over selected 2.5° oceanic (Pacific atoll) grid cells, from Comprehensive Pacific Rainfall Database rain gauges, $MIRA_{[BUC]}$, $UAGPI_{[BUC]}$, and GPI.

rainfall estimates at the pixel scale. For operational applications where estimates are required in real time, such as hydrological modeling, hazard warning, or NWP model initialization, a ''rolling'' calibration window can be utilized. By this method MIRA calibration is based on IR and PMW data from some period immediately prior to the estimate time (Todd et al. 1999).

Since errors in PMW estimation of the rainfall distribution within the calibration domain are maintained in MIRA estimates, there is a clear need to further improve the accuracy of PMW algorithms for incorporation into combined techniques. A potential limitation of MIRA in the form evaluated here is likely to be the bias associated with inadequate sampling of the diurnal rainfall cycle by the SSM/I. To address this, the authors intend to evaluate the performance of MIRA incorporating Tropical Rainfall Measuring Mission (TRMM) precipitation radar (PR) data. Given that the temporal sampling of TRMM PR is poorer than that of the SSM/I, but that estimates of rain rate are likely to be more

accurate, the benefits of a combined IR/TRMM algorithm such as MIRA are likely to be even greater.

Finally, the work highlights the need for accurate validation data at high spatial and temporal resolutions. A full evaluation of the limitations of the algorithm must await the development of such products. The Surface Reference Data Center is currently in the process of developing a 1° daily gauge rainfall product using the auspices of the World Climate Research Program GPCP program.

Acknowledgments. The authors are grateful to the University of Oxford for funding. The authors would also like to thank the International Satellite Cloud Climatology program (ISCCP), the Goddard Institute for Space Studies for production of the ISCCP data, and the Distributed Active Archive Center at the NASA Langley Research Center, EOSDIS, for distribution of ISCCP DX data. These activities are sponsored by NASA's Mission to Planet Earth. PIP-3 data were obtained from the Marshall Space Flight Center.

REFERENCES

Adler, R. F., A. J. Negri, P. R. Keehn, and I. M. Hakkarinen, 1993: Estimation of monthly rainfall over Japan and surrounding waters from a combination of low-orbit microwave and geosynchronous IR data. *J. Appl. Meteor.,* **32,** 335–356.

Anagnostou E. N., A. J. Negri, and R. F. Adler, 1999: A satellite infrared technique for diurnal rainfall variability studies. *J. Geophys. Res.,* **104** (D24), 31 477–31 488.

Arkin, P. A., and B. N. Meisner, 1987: The relationship between large-scale convective rainfall and cold cloud over the Western Hemisphere during 1982–82. *Mon. Wea. Rev.,* **115,** 51–74.

——, R. Joyce, and J. E. Janowiak, 1994: The estimation of global monthly mean rainfall using infrared satellite data: The GOES Precipitation Index (GPI). *Remote Sens. Rev.,* **11,** 107–124.

Atlas, D., and T. L. Bell, 1992: The relation of radar to cloud area–time integrals and implications for rain measurements from space *Mon. Wea. Rev.,* **120,** 1997–2008.

——, D. Rosenfeld, and D. B. Wolff, 1990: Climatologically tuned reflectivity–rainrate relations and links to area-time integrals. *J. Appl. Meteor.,* **29,** 1120–1135.

Barrett, E. C., and M. J. Beaumont, 1994: Satellite rainfall monitoring: An overview. *Remote Sens. Rev.,* **11** (1–4), 49–60.

Dewhurst, N., E. C. Barrett, M. J. Beaumont, and M. C. Todd, 1996: Satellite monitoring of rainfall and surface water balances—In search of the optimum rain/no rain boundary. *Progress in Environmental Remote Sensing Research and Applications,* E. Parlow, Ed., Balkema, 486 pp.

Doneaud, A. A., S. I. Niscov, D. L. Priegnitz, and P. L. Smith, 1984: The area–time integral as an indicator for convective rain volumes. *J. Climate Appl. Meteor.,* **23,** 555–561.

Ebert, E. E., and M. J. Manton, 1998: Performance of satellite rainfall estimation algorithms during TOGA COARE. *J. Atmos. Sci.,* **55,** 1537–1557.

Ferraro, R. R., F. Z. Weng, N. C. Grody, and A. Basist, 1996: An eight-year (1987–1994) time series of rainfall, clouds, water vapor, and sea ice derived from SSM/I measurements. *Bull. Amer. Meteor. Soc.,* **77,** 891–905.

GEWEX, 1996: GPCP Working Group on Data Management, 10th session. *GEWEX News,* August 1996, 8–9.

Huffman, G. J., and Coauthors, 1997: The Global Precipitation Climatology Project (GPCP) combined precipitation dataset. *Bull. Amer. Meteor. Soc.,* **78,** 5–20.

——, R. F. Adler, M. M. Morrissey, S. Curtis, R. Joyce, B. McGavock, and J. Susskind, 2001: Global precipitation at one-degree daily resolution from multisatellite observations. *J. Hydrometeor.,* **2,** 36–50.

Kidd, C. K., 1997: Satellite identification of radar artefacts in rainfall retrievals. *Proc. 23d Conf. on Remote Sensing Society,* Reading, U.K., Remote Sensing Society, 487–492.

——, D. Kniveton, and E. C. Barrett, 1998: Advantage and disadvantages of statistical/empirical satellite estimation of rainfall. *J. Atmos Sci.,* **55,** 1576–1582.

Kummerow, C., and L. Giglio, 1995: A method for combining passive microwave and infrared rainfall observations. *J. Atmos. Oceanic Technol.,* **12,** 33–45.

Lebel, T., and A. Amani, 1999: Rainfall estimation in the Sahel: What is ground truth? *J. Appl. Meteor.,* **38,** 555–568.

Morrissey, M. L., and J. E. Janowiak, 1996: Sampling-induced conditional biases in satellite climate-scale rainfall estimates. *J. Appl. Meteor.,* **35,** 541–548.

——, M. A. Shafer, M. Hauschild, M. Reiss, B. Rudolph, W. Reuth, and U. Scheider, 1994: Surface data sets used in WetNet's PIP-1 from the Comprehensive Pacific Rainfall Data Base and the Global Precipitation Climatology Centre. *Remote Sens. Rev.,* **11** (1–4), 61–92.

Petty, G. W., 1999: Prevalence of precipitation from warm-topped clouds over eastern Asia and the western Pacific. *J. Climate,* **12,** 220–229.

Richards, F., and P. Arkin, 1981: On the relationship between satellite-observed cloud cover and precipitation. *Mon. Wea. Rev.,* **109,** 1081–1093.

Rossow, W. B., and R. A. Schiffer, 1991: ISCCP cloud data products. *Bull. Amer. Meteor. Soc.,* **72,** 2–20.

Smith, D. M., D. R. Kniveton, and E. C. Barrett, 1998: A statistical modelling approach to passive microwave rainfall retrieval. *J. Appl. Meteor.,* **37,** 135–154.

Todd, M. C., and R. Washington, 1999: A simple method to retrieve 3-hourly estimates of global tropical and subtropical precipitation from International Satellite Cloud Climatology Program (ISCCP) D1 data. *J. Atmos. Oceanic Technol.,* **16,** 146–155.

——, E. C. Barrett, M. J. Beaumont, and J. Green, 1995: Satellite identification of rain days over the upper Nile River basin using an optimum infrared rain/no rain threshold temperature model. *J. Appl. Meteor.,* **34,** 2600–2611.

——, ——, ——, and T. J. Bellerby, 1999: Estimation of daily rainfall over the upper Nile river basin using a continuously calibrated satellite infrared technique. *Meteor. Appl.,* **5,** 1–10.

Washington, R., and M. C. Todd, 1999: Tropical temperate links in southern African and southwest Indian Ocean daily rainfall. *Int. J. Climatol.,* **19,** 1601–1616.

Xie, P., and P. A. Arkin, 1997: Global precipitation: A 17-year monthly analysis based on gauge observations, satellite estimates, and numerical model outputs. *Bull. Amer. Meteor. Soc.,* **78,** 2539–2558.

Xu, L., X. Gao, S. Sorooshian, and P. A. Arkin, 1999: A microwave infrared threshold technique to improve the GOES Precipitation Index. *J. Appl. Meteor.,* **38,** 569–579.